Strong terahertz field generation, detection, and application

K. Y. Kim
Institute for Research in Electronics and Applied Physics, University of Maryland, Building 223, Paint Branch Drive, College Park, MD 20742, USA

Email: kykim@umd.edu

Abstract. This report describes the generation and detection of high-power, broadband terahertz (THz) radiation with using femtosecond terawatt (TW) laser systems. In particular, this focuses on two-color laser mixing in gases as a scalable THz source, addressing both microscopic and macroscopic effects governing its output THz yield and radiation profile. This also includes the characterization of extremely broad THz spectra extending from microwaves to infrared frequencies. Experimentally, my group has generated high-energy (tens of microjoule), intense (>8 MV/cm), and broadband (0.01~60 THz) THz radiation in two-color laser mixing in air. Such an intense THz field can be utilized to study THz-driven extremely nonlinear phenomena in a university laboratory.

Contents

1. Introduction: T-rays

Sandwiched between the optical and microwave regimes, the far infrared or terahertz (1 THz = 10^{12} Hz) frequency range has recently drawn special attention due to its ubiquitous nature and broad applications (see Fig. 1) [1-3]. The physics of THz generation is also compelling, raising fundamental questions about the interaction of strong electromagnetic fields with atoms and molecules. THz radiation (or T-rays) can easily pass through non-polar materials such as clothing, paper, plastics, wood and ceramics. This property allows many applications in molecular sensing, biomedical imaging and spectroscopy, security scanners, and plasma diagnostics. In particular, THz spectroscopy holds great promise for molecular sensing. Recent work on stem cells shows that T-rays have potential for controlling cellular gene expression [4].

These applications provide strong motivation to advance the state of the art in THz source development. In particular, high-energy THz generation is vital for application in nonlinear THz optics and spectroscopy. Currently, intense THz radiation pulses exceeding tens of micro-Joules can be obtained from large accelerator facilities such as linear accelerators, synchrotrons, and free electron lasers. However, due to the large cost of building and operating those facilities and limited access, there is a present and growing demand for high-energy, compact THz sources at a tabletop scale.

One approach is to use tabletop ultrafast lasers to produce coherent THz radiation via plasma generation in gases, but the physics of the process is not fully understood and requires detailed understanding of strong field ionization processes in atoms and molecules, especially in the nonperturbative regime. In essence, one must understand the evolution of laser-driven electron wavepackets in a strong electric field and their transition from atomic to plasma states. The generation mechanism also requires a full understanding of collective plasma behaviors and coherent radiation processes at high laser intensities. In addition, there are practical issues to address—Can one control and optimize the process to make compact high-power THz sources? What are the limits on generating and detecting ultra-broadband THz radiation? What interesting nonlinear processes can be driven by powerful THz sources? These questions will be addressed in this report.

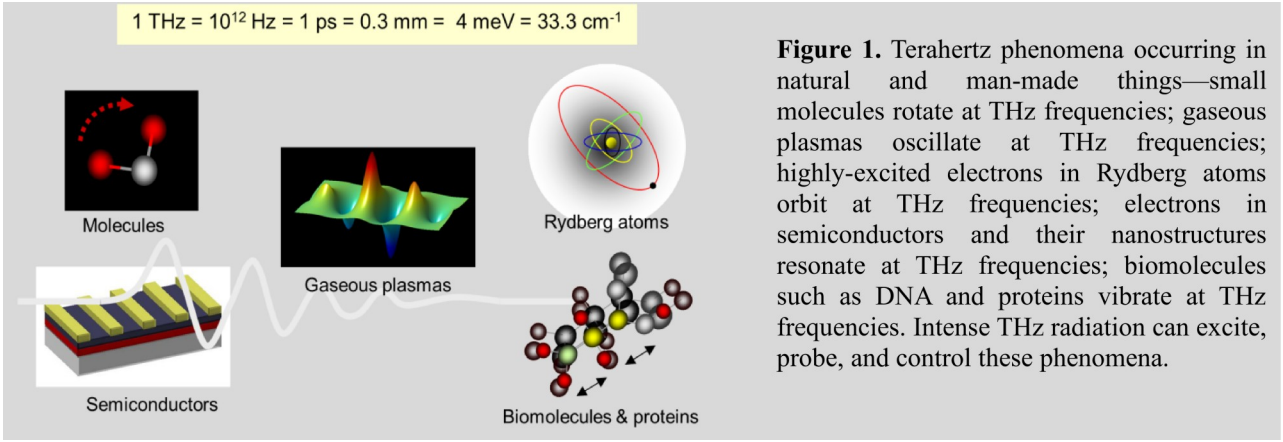

Figure 1. Terahertz phenomena occurring in natural and man-made things—small molecules rotate at THz frequencies; gaseous plasmas oscillate at THz frequencies; highly-excited electrons in Rydberg atoms orbit at THz frequencies; electrons in semiconductors and their nanostructures resonate at THz frequencies; biomolecules such as DNA and proteins vibrate at THz frequencies. Intense THz radiation can excite, probe, and control these phenomena.

2. THz generation via ultrafast two-color laser mixing

Two-color laser mixing (or photoionization) has been widely used as a versatile tool for intense, broadband terahertz (THz) radiation generation [5-34]. In this scheme, an ultrafast pulsed laser's fundamental and second harmonic fields are mixed in a gas of atoms or molecules, causing them to ionize (see Fig. 2). This phenomenon was first observed by D. J. Cook and R. Hochstrasser at University of Pennsylvania in 2000 [5]. Since then, many experiments had followed up for several years without a basic understanding of the process. A four-wave mixing theory was initially proposed to explain the mechanism

[5-9], but it did not provide any microscopic origin of such nonlinearity. Then Kim *et al*., proposed a plasma current model to explain the mechanism of THz generation [10].

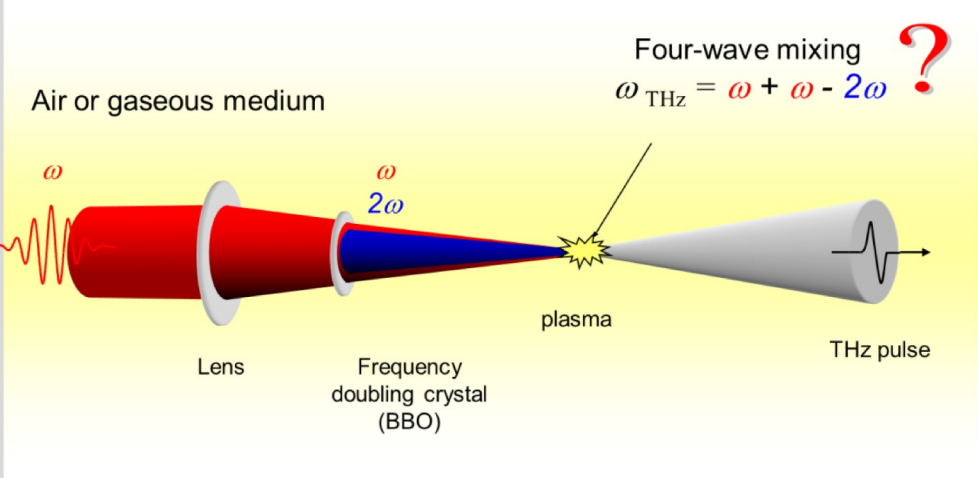

Figure 2. Schematic of THz generation via two-color photoionization in gases. Initially, this THz generation was understood as a four-wave mixing process in a gas medium [5] but it was soon noticed that the third order nonlinearity of gas medium is too small to explain the measured THz field strength [6]. Moreover, further experiments confirmed that the THz output increases dramatically with onset of plasma formation, indicating that plasma plays a key role in THz generation.

In the plasma current model, the laser fields act to suppress the atom's or molecule's Coulomb potential barrier, and, via rapid tunneling ionization, bound electrons are freed. The electrons, once liberated, oscillate at the laser frequencies, and also drift away from their parent ions at velocities determined by the laser field amplitudes and the relative phase between the two laser fields (see Fig. 3). Depending on the relative phase, symmetry can be broken to produce a net directional electron current. As this current occurs on the timescale of photoionization, for sub-picosecond lasers, it can generate electromagnetic radiation at THz frequencies [10-12].

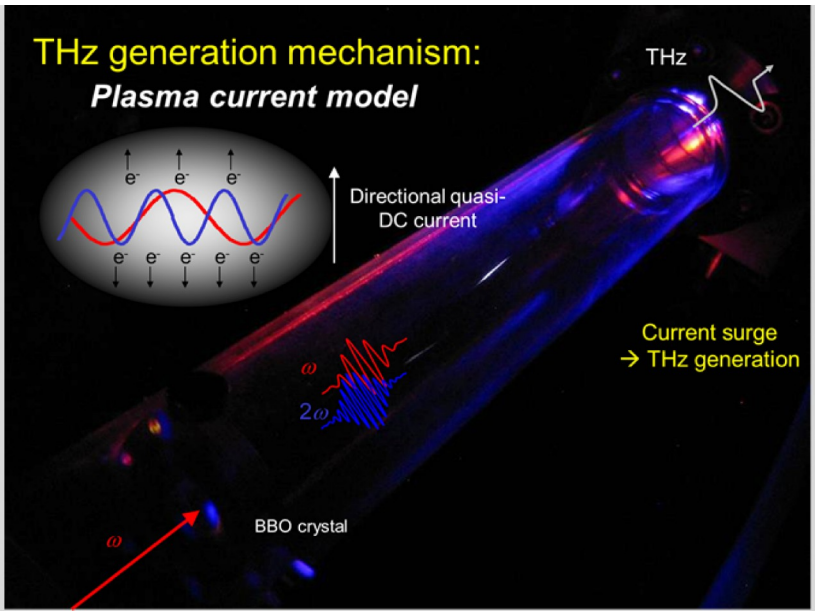

Figure 3. Microscopic plasma current model for THz generation in two-color photoionization. In this model, THz radiation arises from tunneling ionization and subsequent electron motion in a symmetry-broken electric field. This mechanism is closed related to that used to explain high harmonic generation in gases. The electrons re-colliding with the parent ions are responsible for HHG, whereas the electrons drifting away from the ions without experiencing re-scattering ions account for THz generation.

K. Y. Kim, A. J. Taylor, J. H. Glownia, and G. Rodriguez, Optics and Photonics News **19**, 49 (2008).

3. Microscopic model for THz generation

At relatively low laser intensities (<10^{15} W/cm^2), a single-color laser pulse cannot produce a directional current because a half of the liberated electrons drift up and the other half electrons drift down, consequently cancelling out the net current. A non-vanishing directional current, however, can arise and generate THz radiation if an additional laser field (second harmonic) is mixed with the fundamental laser field (see Fig. 4(a)). Here, the combined laser field can be expressed as

$$E_L(t) = E_\omega \cos \omega t + E_{2\omega} \cos(2\omega t + \theta),$$

where E_ω and $E_{2\omega}$ are the amplitudes of the fundamental (ω) and the second harmonic (2ω) fields, respectively, and θ is the relative phase between two fields. Figure 4 shows 1-dimensional simulation results on electron trajectories, plasma currents, and radiation spectra under such a two-color laser field.

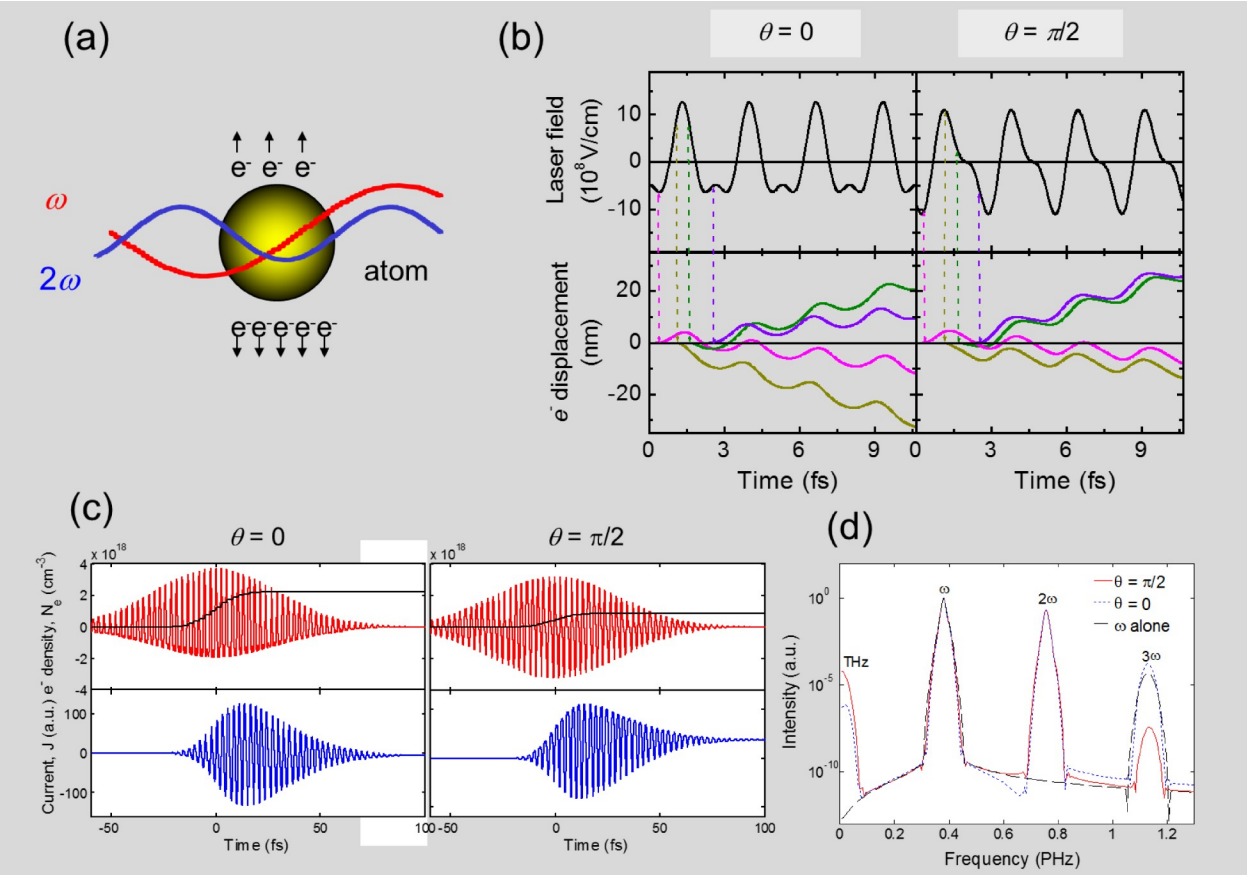

Figure 4. (a) Schematic of tunneling ionization of an atom and subsequent free electron generation and acceleration in a two-color laser field. **(b)** (Top) Two-color laser field consisting of 800 nm (fundamental) and 400 nm (second harmonic) waves with a relative phase θ = 0 and π/2. (Bottom) Electron trajectories born at various phases of $-9\pi/10$, $-\pi/10$, $\pi/10$, and $9\pi/10$. **(c)** (Top) Two-color laser field (red solid line) and free electron density (black line) as a function of time with a relative phase of θ = 0 or θ = π/2, computed at peak laser intensities of I_ω = 10^{14} W/cm^2 at λ_1 = 800 nm and $I_{2\omega}$ = 2 × 10^{13} W/cm^2 at λ_2 = 400 nm with the same pulse duration 50 fs (FWHM, Gaussian temporal profiles). The target gas is atmospheric pressure nitrogen. (Bottom) The corresponding electron current versus time with a relative phase of θ = 0 or θ = π/2. **(d)** Radiation spectra for θ = 0 (blue line) and π/2 (red line), as well as for ω field alone (black line). The quasi-DC peak (THz radiation) is maximal with θ = π/2. There is little THz radiation with θ = 0 and nearly no THz radiation with single-color alone.

4. THz generation and detection

4.1. Energy measurement

Most incoherent THz detectors measure incident THz energy or power by measuring a temperature change induced by THz absorption. Such detectors include bolometers, Golay cells, thermopiles, and pyroelectric detectors. In particular, pyroelectric detectors utilize pyroelectric materials which generate a voltage when they are heated or cooled. This pyroelectric effect arises from spontaneous electric polarization induced by temperature changes. Lithium tantalite ($LiTaO_3$) is a pyroelectric material commonly used for THz detection. Figure 5 shows a typical scheme for THz energy measurement with a pyroelectric detector. Various filters can be used to characterize incident THz spectrum. For example, a silicon wafer can block optical light but transmit THz radiation with wavelength from 1.2 μm to 1000 μm. Teflon or high-density polyethylene (HDPE) acts as a low-pass filter blocking THz frequencies higher than 3 THz. Pyroelectric detectors provide a relatively flat spectral response over a broad range of THz spectrum (3 ~ 30 THz), and they can be calibrated at 800 nm using optical pulses.

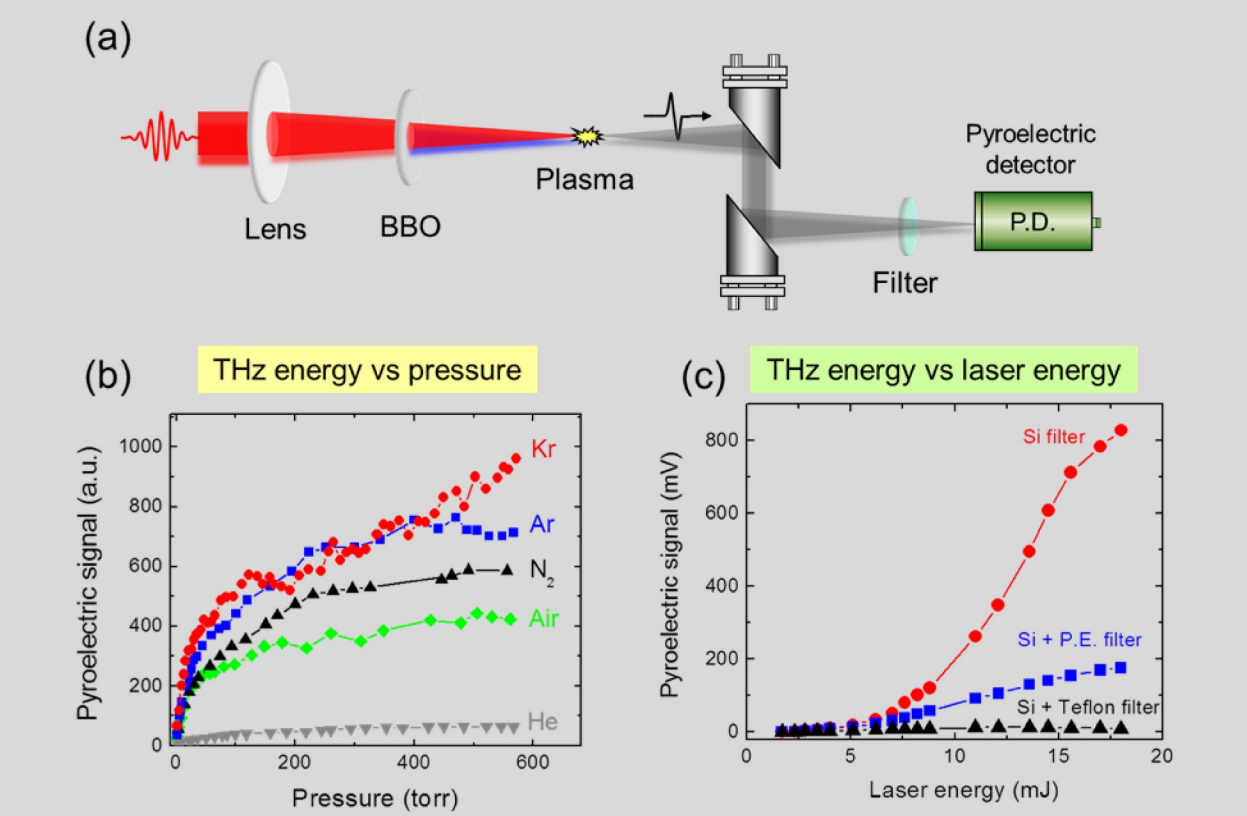

Figure 5. (a) Experimental setup for THz generation via femtosecond two-color laser mixing and detection with a pyroelectric detector. **(b)** Pyroelectric detector signal as a function of backfilled gas pressure for various gas species. The measured THz output (Kr > Ar > N_2 > He) is consistent with the magnitudes of the tunneling ionization rates for these gases. The peak THz energy measured by the pyroelectric detector is >5 μJ with Kr **(c)** Pyroelectric detector signals as a function of incident laser energy, obtained with a 3-mm thick Si THz transmission filter placed in front of the pyroelectric detector, as well as with an additional 1-mm thick polyethylene (PE) or 3-mm thick Teflon filter.

K. Y. Kim, A. J. Taylor, J. H. Glownia, and G. Rodriguez, Nature Photon. **2**, 605 (2008).

4.2. Waveform and spectrum measurement

The measurement of THz waveforms is important in THz time domain spectroscopy for material characterization and biomedical imaging. Electro-optic sampling (EOS) and fast photoconductive switching are two widely used techniques in measuring THz fields. In these techniques, the optical-THz pulse delay is successively varied with respect to the optical probe in order to map out the complete THz waveform from a series of time-delayed snapshots. Figure 6 shows a typical EOS setup for measuring THz waveforms.

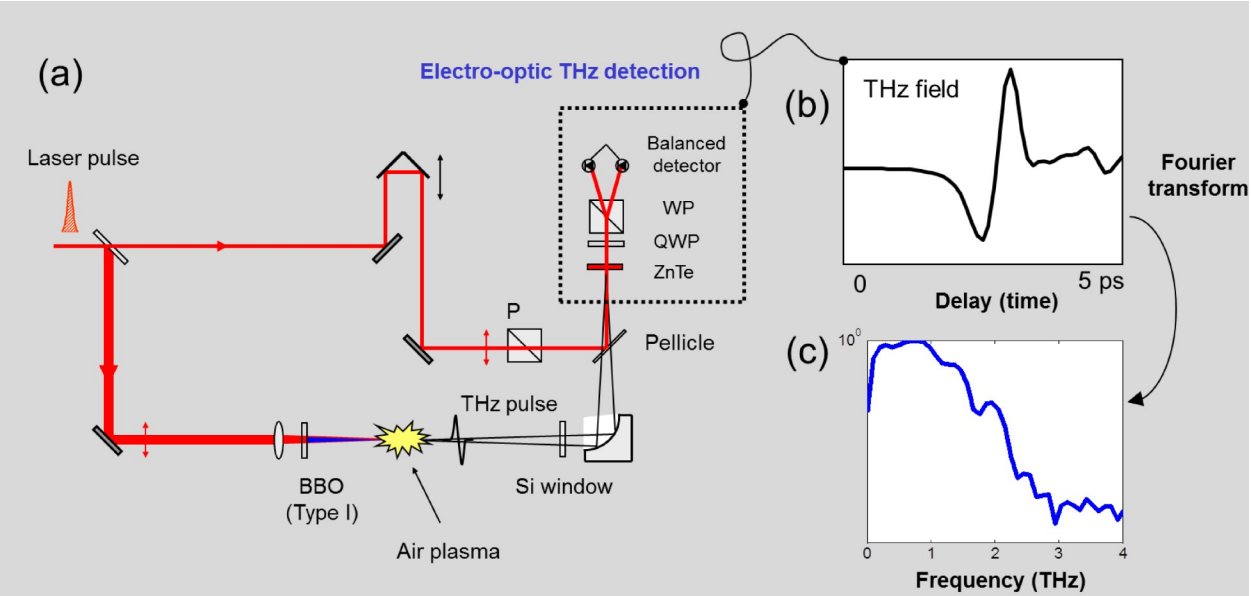

Figure 6. (a) Experimental setup for THz generation via femtosecond two-color photoionization and detection via electro-optic sampling (EOS). The underlying mechanism relies on the Pockels effect in an electro-optic crystal. A static (or THz) field applied across the crystal induces birefringence, proportional to the applied field amplitude. By measuring the birefringence experienced by a probe pulse, one can deduce the applied field strength. In the case where there is no THz pulse, a linearly polarized optical pulse propagates through an EO crystal with no polarization change, and then the polarization becomes circular after a quarter waveplate (QWP). A Wollaston prism (WP) splits the circularly polarized probe into *P*- and *S*-polarized beams. A balanced photo-detector measures the intensity difference of these two beams. When a THz pulse co-propagates with the optical probe into the EO crystal, the THz field acts as a static field and induces a Pockels effect, making the probe beam elliptically polarized. The balanced detector measures the intensity difference between *P*- and *S*-polarized components, which is proportional to the THz amplitude (not intensity). By scanning the delay between the probe and THz pulses, one can map out the entire THz waveform. **(b)** Typical experimental THz waveform obtained with a 1-mm thick ZnTe EO crystal. **(c)** Corresponding THz spectrum obtained via Fourier transformation.

4.3. Waveform measurement in single-shots

Single-shot THz waveform measurement is vital for THz spectroscopic applications involving irreversible processes such as studies of material damage and structural phase transitions, as well for monitoring relativistic ultrashort electron bunch profiles in real time.

One single-shot THz diagnostic, previously demonstrated by Jiang *et al*. [35], adopts a temporally chirped optical probe pulse to map out the entire THz field in a single shot (see Fig. 7(a)). In this scheme, each temporal slice of the THz field is projected onto a different frequency component of the chirped pulse, allowing the entire THz field to be reconstructed from direct mapping of frequency to time. While

this so-called spectral encoding technique has been applied to many experiments, it has also been shown that the temporal resolution is ultimately limited by the extent of the chirp applied to the probe pulse. To overcome the limitation, a novel THz retrieval algorithm was developed which can significantly enhance the temporal resolution in the spectral encoding technique [36]. With the technique, the temporal resolution is ideally limited only by the spectral bandwidth of the chirped probe pulse (see Fig. 7(b)). With an imaging spectrometer, the diagnostic can also provide 1-dimensional spatial information.

Another single-shot THz diagnostic developed by Kim *et al*. is two-dimensional electro-optic imaging with dual echelons [37]. An echelon itself consists of a right-angle prism with a stepwise structure on the hypotenuse surface which can split an incoming single laser pulse into incrementally time-delayed multiple small beamlets, either thru transmission or reflection. With the addition of a second orthogonally-oriented echelon whose single step size matches the overall step height of the first echelon, additional beamlets can be produced with an increased time window. Figure 7(c) shows the result of 2D echelon imaging of THz field in a single-shot. This method can routinely provide a >10 ps time window with ~25 fs temporal step size. By varying the echelon step sizes, the time step and/or field of view can be adjusted for a variety of applications. This method, however, does not provide any spatial information imaging.

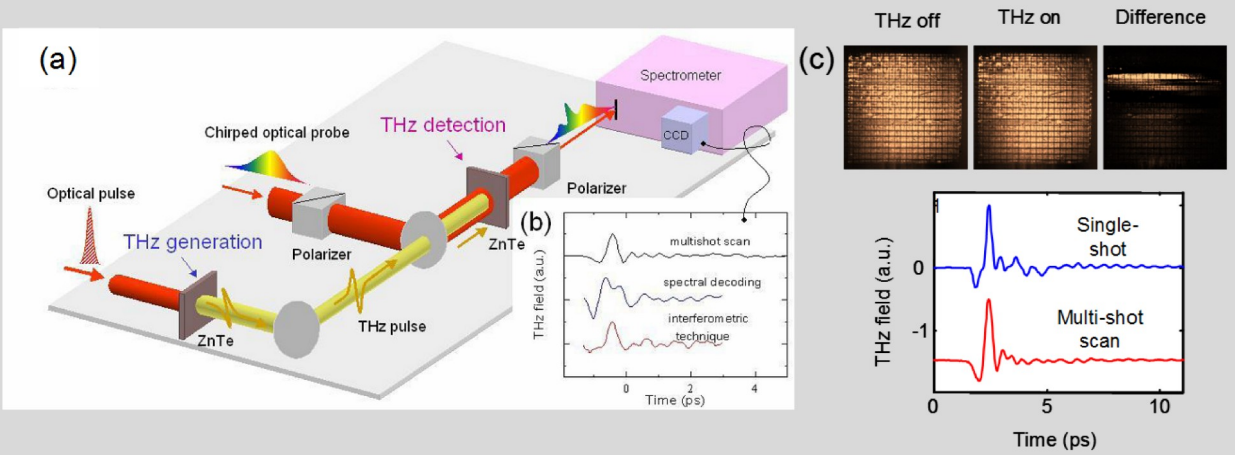

Figure 7. (a) Schematic of THz generation by optical rectification in ZnTe and single-shot THz waveform detection with a chirped laser pulse. The EO effect induced by a THz pulse is encoded onto a chirped optical probe, and its spectral modulation is detected by a spectrometer. **(b)** THz waveforms obtained by multi-shot scan, spectral encoding, and interferometric techniques, respectively [36]. **(c)** Echelon images with comparison of THz waveforms obtained with single-shot and conventional multi-shot scanning [37].

K. Y. Kim **et al**., Appl. Phys. Lett. **88**, 041123 (2006); K. Y. Kim **et al**., Opt. Lett. **32**, 1968 (2007).

4.4. Waveform measurement via THz-EFISH

Another method for broadband detection is using electric-field-induced second-harmonic (EFISH), also known as air-biased-coherent-detection (ABCD) [9]. In this scheme, the THz pulse to be characterized is collimated and focused into air along with an ultrashort optical pulse (800 nm), which produces an optical second harmonic (400 nm) by the EFISH effect (see Fig. 8(a)). This can be considered as the reverse process of THz generation by two-color mixing in air. Here, the change in second harmonic yield is proportional to the THz electric field to be measured at the focus [9]. One big advantage of this technique is its capability of detecting THz waveforms directly. However, the detection bandwidth is fundamentally limited by the probe pulse duration. In our laboratory, we have measured THz radiation up to 30 THz (see Fig. 8(c)), currently limited by our stretched probe pulse width (30 fs ~ 40 fs) and/or the size of the electrodes used for ABCD detection.

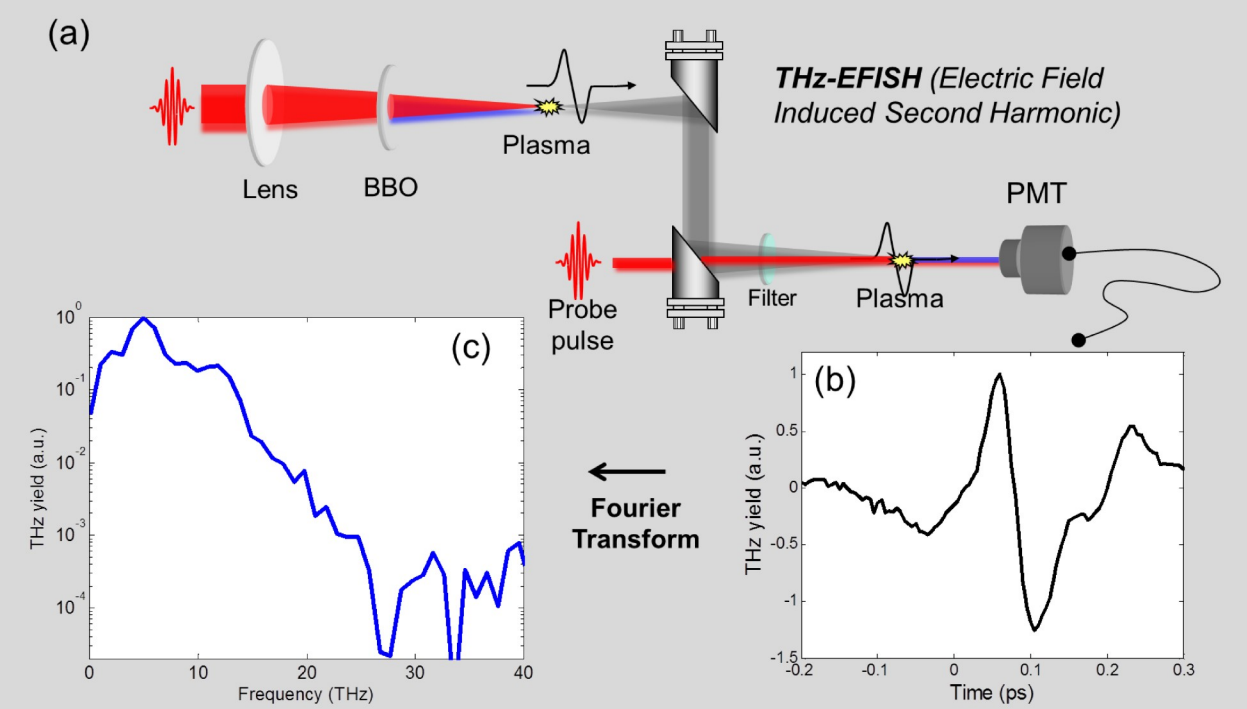

Figure 8. (a) Experimental setup for THz generation via femtosecond two-color photoionization and detection via THz electric field induced second harmonic (THz-EFISH). At the focus, the THz field induces a second harmonic (400 nm) of the probe beam (800 nm). The induced second harmonic is detected by a photomultiplier tube (PMT) with narrow-band interference filters placed in front. **(b)** Typical THz waveform and **(c)** its spectrum.

4.5. Spectrum measurement via Fourier transform interferometry

For even higher bandwidth detection, Michelson interferometery can be utilized for Fourier transform infrared (FTIR) spectroscopy. The THz pulses to be measured are split and recombined by a beamsplitter and then they interfere with a relative phase set by the optical path length difference between the two arms (see Fig. 9(a)). The interference measured by a pyroelectric detector is Fourier transformed to frequency-domain for THz spectral intensity information (see Fig. 9(b)). Although FTIR does not directly provide THz waveforms, the detection bandwidth is not limited by the optical probe duration as in EFISH.

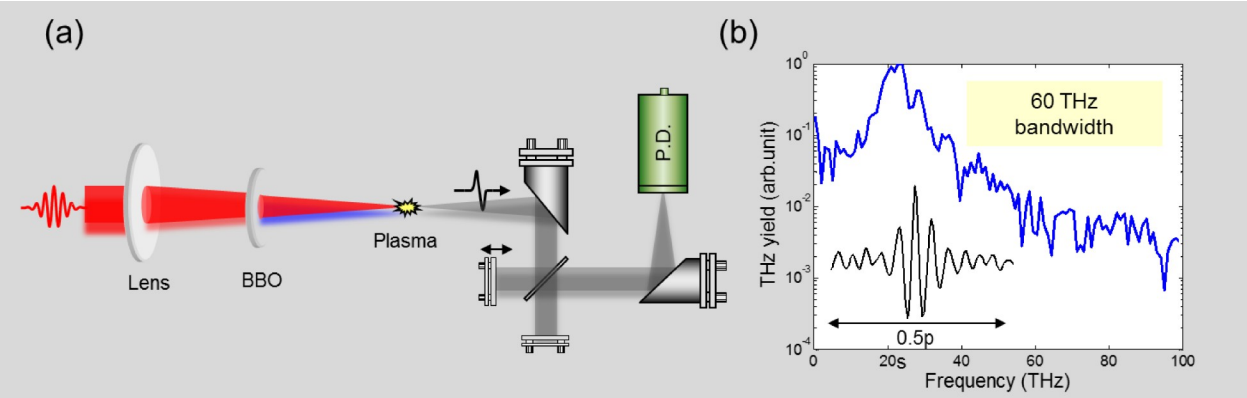

Figure 9. (a) Terahertz spectral measurement with Michelson interferometry. **(b)** Typical first-order

interferometric field autocorrelation and its corresponding THz spectrum measured by Fourier transform infrared spectroscopy (FTIR). It shows radiation up to ~60 THz with input pulse duration of ~30 fs.

4.6. Broadband THz characterization

Two-color photoionization can generate EM radiation at an extreme broad range covering from RF to extreme ultraviolets (EUVs). At first, an ultrafast photocurrent induced by two-color ionization creates EM radiation with a large bandwidth. Here the timescale for the current surge is much shorter than the laser pulse duration because tunneling ionization occurs mostly around the peak intensity. For a ~30 fs (FWHM) laser pulse width, for example, the total ionization process extends over as short as ~12 fs (FWHM). This supports EM radiation with a bandwidth of >80 THz. This radiation bandwidth is further broadened and modulated by several mechanisms summarized in Fig. 10(a).

First, the laser spectrum broadens with propagation due to self-phase modulation in air, ionization-induced blueshifts and self-steepening. The broadened laser spectrum increases the THz bandwidth even further. The spectrum at 0.1~1 THz is strongly modulated by plasma oscillation and collisional effects. In addition, the plasma density of 10^{16} ~ 10^{17} cm^{-3} strongly affects THz absorption in the filament direction. The collisional process ultimately terminates the plasma current. However, a very slow ion current can arise, producing radiation down to 0.01 THz. This corresponds to RF and micro waves. At the other frequency end, broadband EUVs can be produced by optical high harmonic generation (HHG). In particular, two-color based HHG can produce both odd and even harmonics, also enhancing the overall yields. This HHG is strongly connected with THz generation as they both arise from coherent motion of electrons in tunneling ionization. To detect such broadband radiation, various complementary methods must be applied. Figure 10(b) summarizes our THz detection schemes along with their measured radiation spectra.

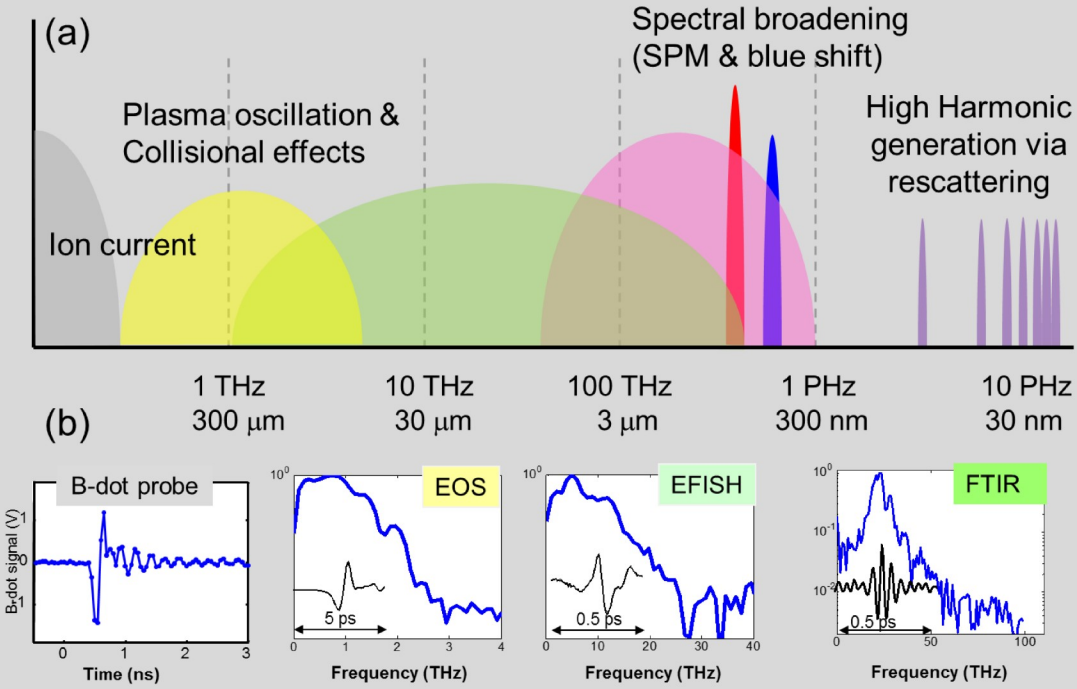

Figure 10. (a) Mechanisms for broadband electromagnetic radiation generation in two-color photoionization and radiation spectra measured with the **(b)** B-dot probe, EOS in ZnTe, EFISH, and FTIR techniques at broad frequency ranges (see Sections 4.2, 4.4, and 4.5). The B-dot probe detects extremely low frequency components such as RF and microwaves. The figure above shows a sub-nanosecond electric current detected with a B-dot probe.

T. I. Oh, Y. S. You, N. Jhajj, E. Rosenthal, H. M. Milchberg, and K. Y. Kim, New J. Phys. **15**, 075002 (2013).

5. THz generation mechanisms

5.1. Microscopic origin

Regarding the mechanism of THz generation in two-color photoionization, two models have been presented so far: four-wave mixing [5, 8] and plasma current model [10-12]. In the four-wave mixing model, THz emission arises from the rectified (quasi-DC) polarization of atomic or molecular bound electrons in two-color laser fields, which can be expressed as

$$P(\omega+\omega-2\omega) \propto \chi^{(3)} \left| \tilde{E}_{\omega} \tilde{E}_{\omega} \tilde{E}_{2\omega} \right| \cos(\theta)$$

Here $\chi^{(3)}$ is the third order susceptibility of the atom, and $E_{\omega}(t)=\tilde{E}_{\omega}(t)\cos(\omega t)$ $E_{2\omega}(t)=\tilde{E}_{2\omega}(t)\cos(2\omega t+\theta)$ are the laser fields of the fundamental (ω) and second harmonic (2ω) waves, and θ is the relative phase between those two waves. By contrast, the plasma current model predicts that THz emission originates from a directional electron current produced by photoionization in a temporally asymmetric laser field arising from two-color laser pulses [10-12]. The predictions made by these two models contradict each other such that maximal THz generation is predicted at $\theta = 0$ (or π) in four-wave mixing whereas at $\theta = \pi/2$ (or $3\pi/2$) in plasma current generation.

To verify such a microscopic detail, a direct measurement of the optimal relative phase θ is necessary. In most experiments involving two-color laser pulses, the relative phase θ is not measured directly. Rather, it is indirectly inferred from models. To avoid this ambiguity, we apply a dichroic interferometry method [38-40] to directly measure the relative phase θ. Simultaneously, we observe plasma currents arising in the vicinity of the focus where THz radiation originates (see Fig. 11). These measurements are conducted for different gas species, laser intensities, and two-color amplitude ratios in order to have a comprehensive understanding of the microscopic origin of THz emission.

We have confirmed that the optimal relative phase for THz generation is ~$\pi/2$, not significantly affected by gas species, laser intensities, and intensity ratios between two-color laser fields. These results are in accordance with the semi-classical plasma current model [10-12]. This verifies plasma currents as a microscopic source for far-field THz radiation in two-color laser-produced plasmas.

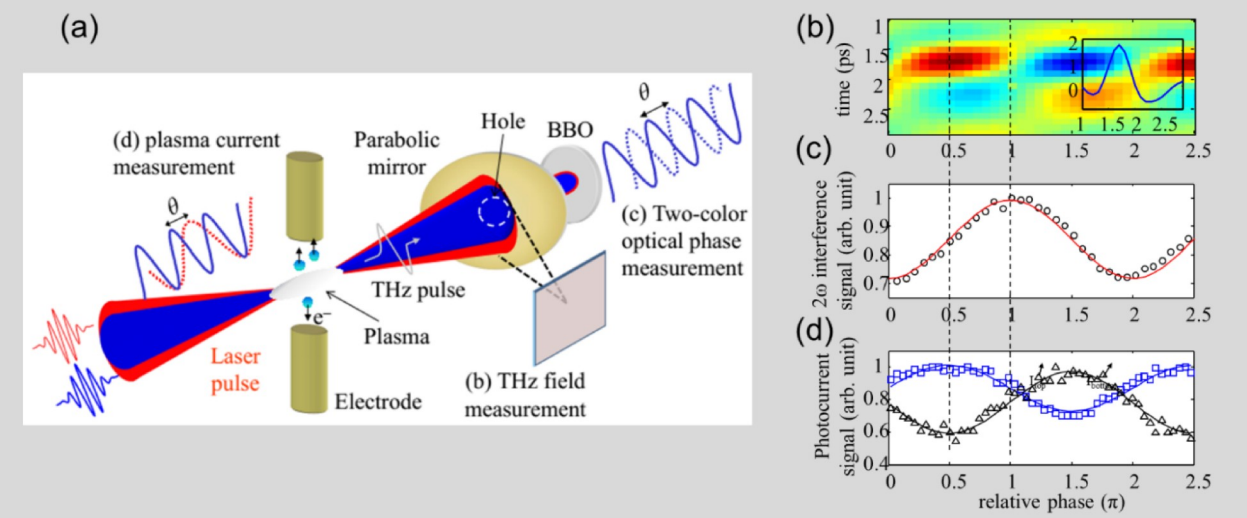

Figure 11. (a) Schematic setup with measured **(b)** time-domain THz, **(c)** 2ω interference (circles), and **(d)** plasma current (squares and triangles) signals. The inset in (b) shows a typical THz waveform obtained at a relative phase of π/2, calibrated by the 2ω interference measurement in (c). The red, blue, black curves are fittings. The vertical dotted lines indicate minimal and maximal THz and plasma current generation at 0.5π and π,

respectively.

Y. S. You, D. Zhang, T. C. Rensink, J. Palastro, T. M. Antonsen Jr., and K. Y. Kim, Phys. Rev. Lett. (submitted).

5.2. Macroscopic effect: Cherenkov radiation-like phase matching

In general, THz radiation produced by two-color laser mixing shows conical structures (see Fig. 12(d)). This originates from two types of macroscopic phase matching effects—Cherenkov-type radiation [33] and off-axis phase matching [21]. Cherenkov-type phase matching arises when the radiation source (filament) moves faster than the speed of THz radiation (see Fig. 12). For relatively short filaments, typically <10 mm, Cherenkov-type phase matching is dominant and can explain such conical emission.

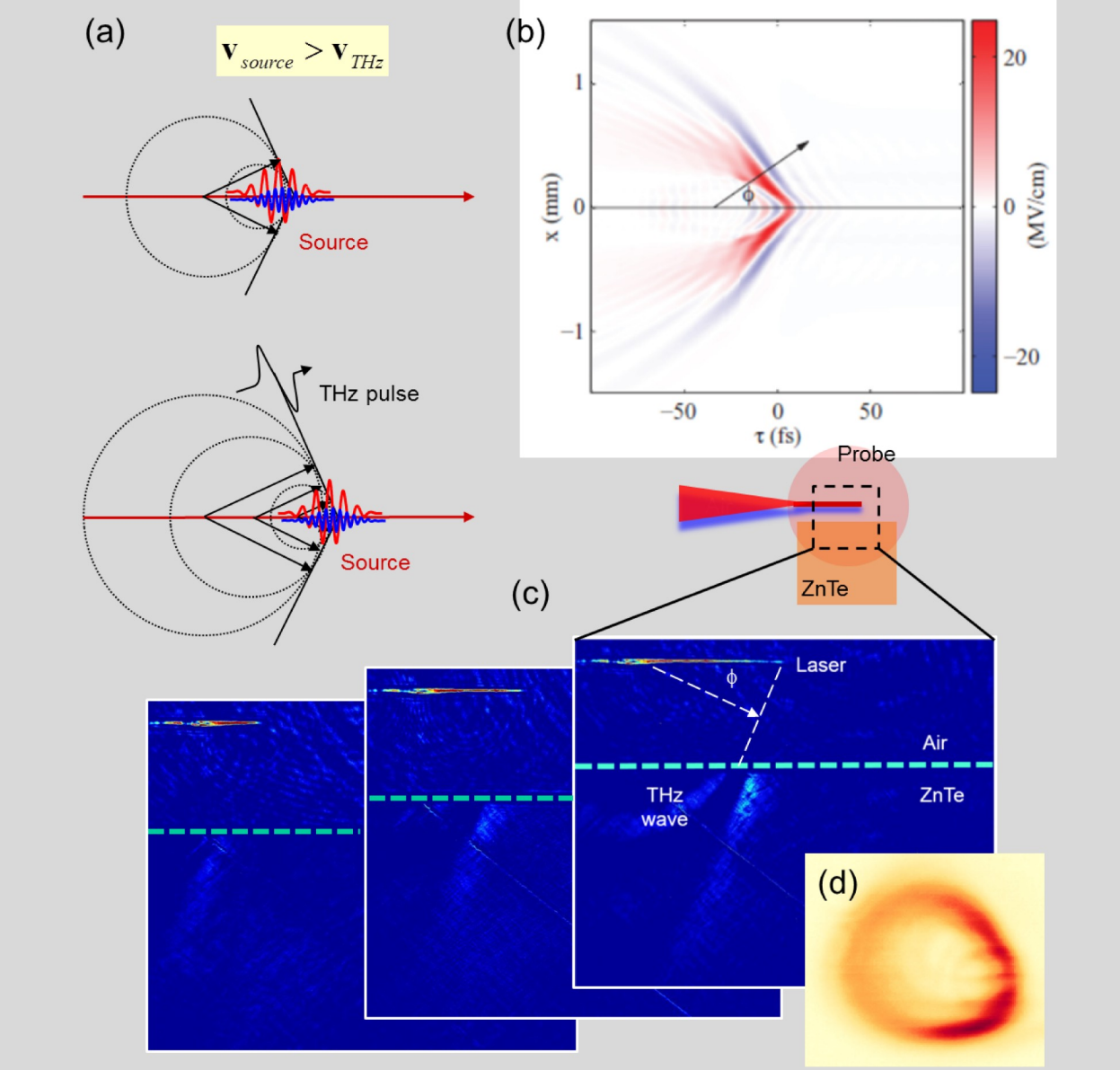

Figure 12. (a) Schematic of Cherenkov radiation-like phase matching due to a radiation source (plasma filament) moving faster than the speed of THz radiation. **(b)** Simulated electric field from 0 to 100 THz at 2 cm before vacuum focus. **(c)** Experimental diagram with time-delayed images showing a moving laser-produced filament

(source) and its resulting THz radiation striking the Air-ZnTe boundary. **(d)** Conical THz emission in the forward direction imaged by a microbolometer camera (see Section 6.5).
L. A. Johnson, J. P. Palastro, T. M. Antonsen, and K. Y. Kim, Phys. Rev. A **88**, 063804 (2013).

5.3. Macroscopic effect: off-axis phase matching

In two-color laser mixing, the resulting THz radiation amplitude is sensitive to the relative phase, θ, between the ω and 2ω pulses in the plasma, where the THz amplitude scales as $E_{\mathrm{THz}} \propto \sin\theta$ [5-10]. However, long plasma filaments ranging from a few centimeters to tens of meters can be formed via femtosecond filamentation in air [41-45]. In this case, the relative phase θ varies along the filament due to dispersion, which modulates the amplitude and polarity of local THz waves. Because of this, no THz enhancement was previously predicted in the forward direction [16].

However, phase-matching naturally occurs due to off-axis constructive interference between locally generated terahertz waves, and this determines the far-field terahertz radiation profiles and yields [21]. For a filament longer than the characteristic two-color dephasing length (≈22 mm), it emits conical terahertz radiation in the off-axis direction, peaked at 4~7° depending on the radiation frequencies. The total terahertz yield continuously increases with the filament length, well beyond the dephasing length. The phase-matching condition observed here provides a simple method for scalable terahertz generation in elongated plasmas.

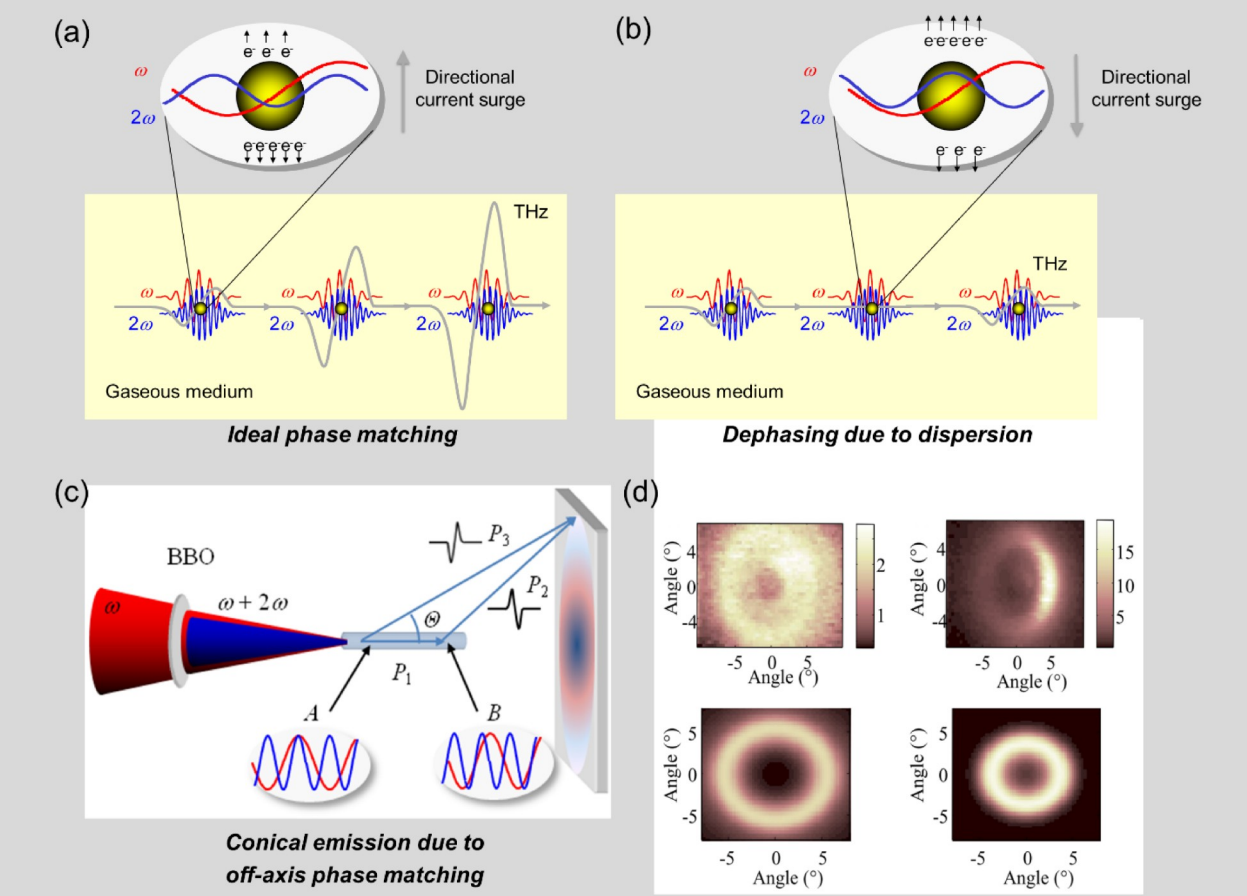

Figure 13. (a) Ideal phase matching for THz generation in an extended medium, which is not satisfied by material dispersion as in **(b)**. **(c)** Schematic of off-axis phase matched THz emission from a long, two-color laser-produced filament. The phase slippage between 800 nm (red) and 400 nm (blue) pulses along the filament results in a periodic oscillation of microscopic current amplitude and polarity. The resulting far-field THz

radiation is determined by interference between the waves emitted from the local sources along the filament. This yields conical THz radiation profiles as in **(d)**. (Top) Experimental and (Bottom) simulated THz radiation profiles.

Y. S. You, T. I. Oh, and K. Y. Kim, Phys. Rev. Lett. **109**, 183902 (2012).

6. Recent experiments

6.1. Energy scaling with extended filamentation

Femtosecond laser pulses often create filaments ranging from a few centimeters to meters due to dynamic balancing between Kerr-induced laser self-focusing in air and plasma-induced defocusing [41-45]. In this filamentation regime, it is of great interest to understand what limits THz output energy and how the yield can be optimized. In this regard, we have examined THz energy scaling and saturation in two-color filamentation with laser energy up to 60 mJ. In particular, we have investigated laser energy coupling into filaments under various external focusing conditions (see Fig. 14), ultimately addressing a mechanism leading to THz yield saturation. We find that saturation occurs mainly due to ionization-induced defocusing and laser intensity clamping in filamentation. Because of this, the laser energy is not effectively coupled into plasma. To minimize such effects and thus improve the THz conversion efficiency, one can distribute the laser energy over a longer filament benefiting from off-axis THz phase-matching.

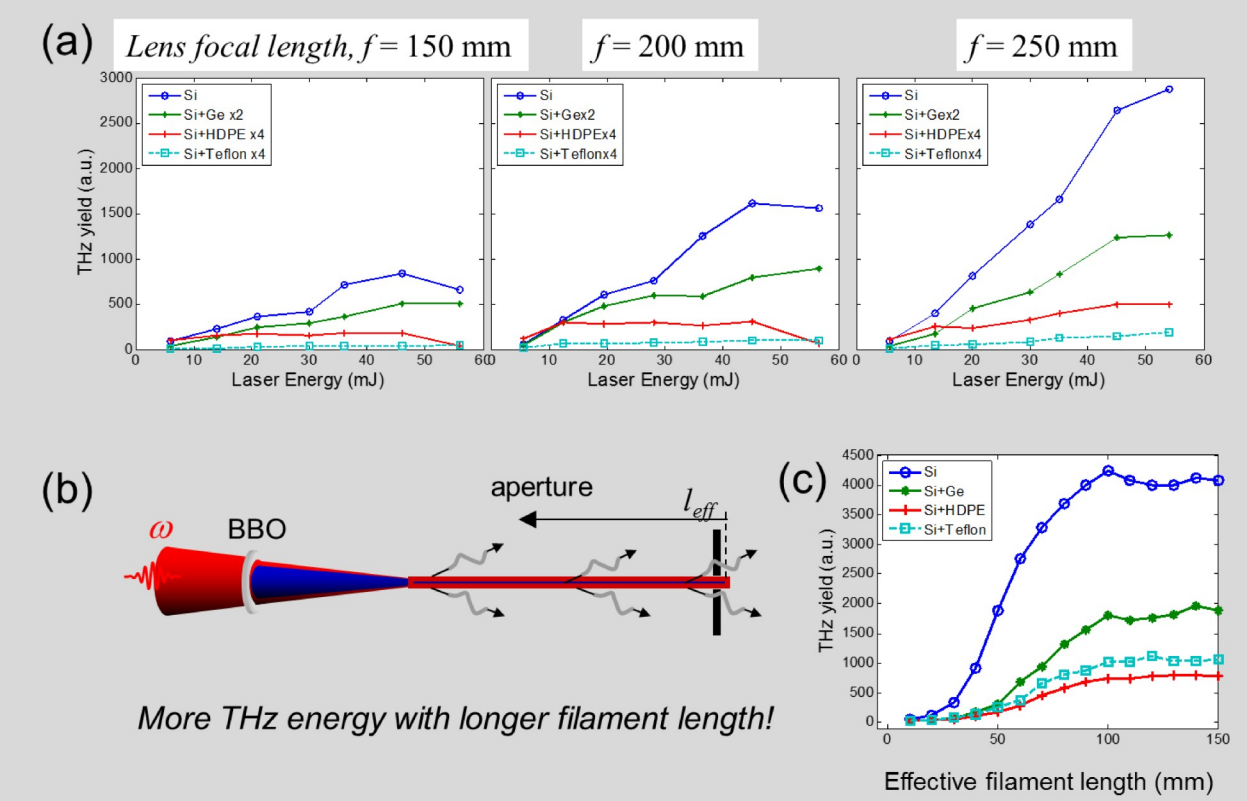

Figure 14. (a) Measurements of THz output energy (pyroelectric detector signal) obtained with various THz filters (Si, Ge, HDPE, and Teflon) as a function of input laser energies with three different focusing lenses: f = 150 mm, f = 200 mm, and f = 250 mm. The Si-Ge and Si-HDPE curves are multiplied by 2 and 4, respectively, for clarity. **(b)** Experimental setup for measuring far-field THz yield as a function of the plasma filament length controlled by a scanning aperture. **(c)** Output THz yields obtained with various filters (Si, Si-Ge, Si-HDPE, and Si-Teflon) as a function of increasing filament length ($\mathbf{l}_{eff}$) for a focal-length of f = 1.0 m.

T. I. Oh, Y. S. You, N. Jhajj, E. Rosenthal, H. M. Milchberg, and K. Y. Kim, Appl. Phys. Lett. **102**, 201113 (2013).

6.2. THz polarization and yield control via 2-dimensional plasma currents

Most two-color photoionization experiments adopt an all-in-line second harmonic and THz generation arrangement as shown in Fig. 15(a). In this scheme, the BBO crystal needs to be azimuthally oriented such that the ω field has a component parallel to the 2ω field polarized in the extraordinary ($\hat{\mathbf{e}}$) axis of the BBO crystal. In this case, the fundamental pulse becomes elliptically polarized after passing through the crystal whereas the second harmonic remains polarized along the extraordinary axis (see Fig. 15(b)). This setting invokes two-dimensional (2-D) transverse electron currents for THz generation. Here, we extend our microscopic plasma current model into 2-D to examine laser parameters in controlling THz yields and polarization, as well as finding optimized conditions for THz generation (see Fig. 15(c)) [20].

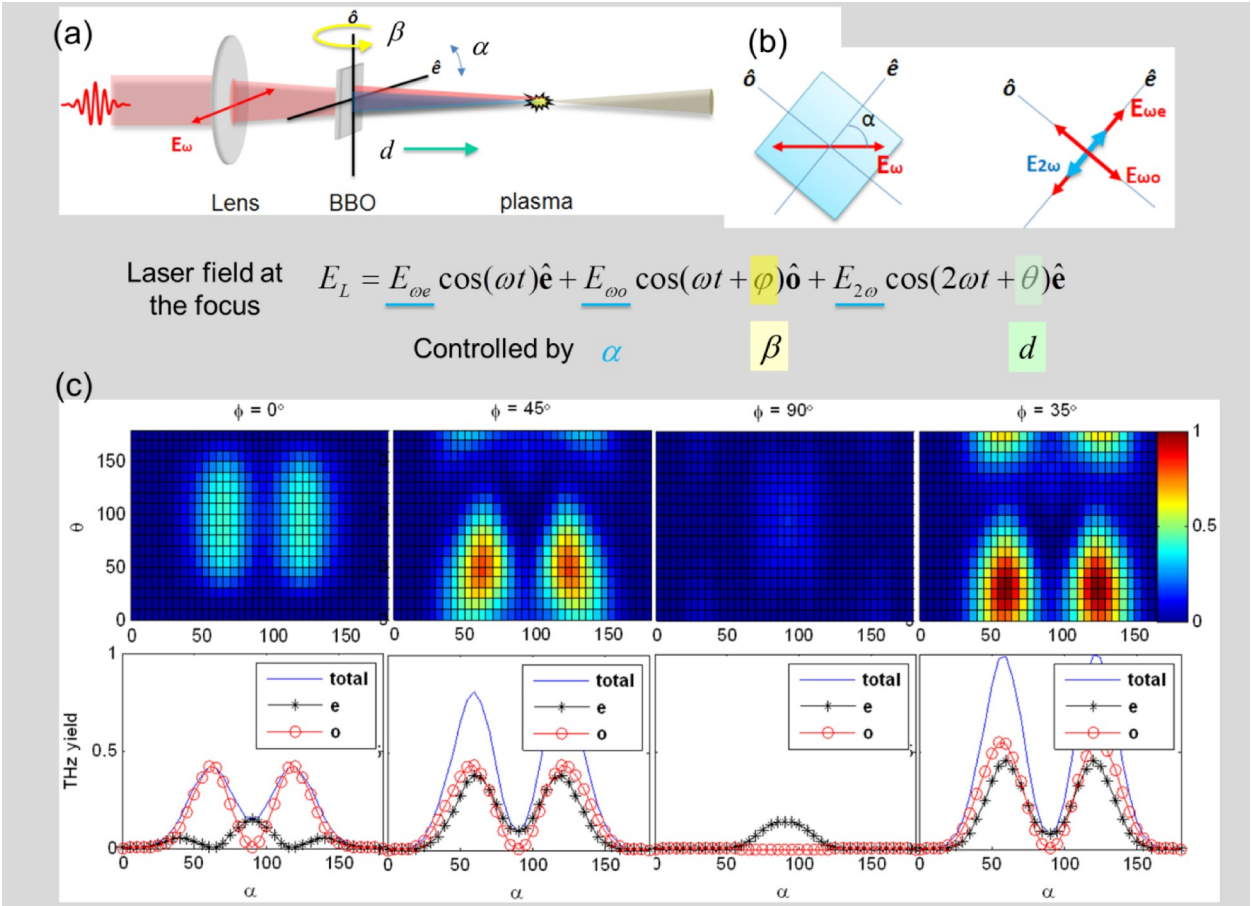

Figure 15. (a) Schematic of all-in-line second harmonic and THz generation. **(b)** Vector diagram for fundamental (E_ω) and its second harmonic ($E_{2\omega}$) generation before the BBO crystal and at the front end of plasma filament. $\hat{\mathbf{o}}$ and $\hat{\mathbf{e}}$ represent the ordinary and extraordinary axes of the BBO crystal respectively. $E_{\omega o}$ and $E_{\omega e}$, polarized along the ordinary ($\hat{\mathbf{o}}$) and extraordinary ($\hat{\mathbf{e}}$) axes of the crystal. **(c)** (Top) Simulated $|\boldsymbol{J}_\perp|^2$ (or THz yield) as a function of θ and α (degrees) for four different φ = 0˚, 45˚, 90˚, and 210˚. (Bottom) In each 2-D simulation, the line which yields the local $|\boldsymbol{J}_\perp|^2$ maximum at a fixed θ is selected and plotted as a function of α for $|J_o|^2$ (line with circles), $|J_e|^2$ (line with asterisks), and $|\boldsymbol{J}_\perp|^2$ (solid line).

T. I. Oh, Y. S. You, and K. Y. Kim, Opt. Express **20**, 19778 (2012).

6.3. Elliptically polarized THz generation

In Section 6.2, THz polarization is understood in the context of 2-dimensional (2D) plasma current model in which two orthogonal plasma currents driven by the laser fields determine the far-field THz amplitude and polarization [20]. This microscopic (single-atom) model, however, predicts THz radiation solely polarized along the direction of the current vector sum.

Here, we extend the 2D plasma current model by including a macroscopic laser-THz propagation effect, which provides a basis for elliptically polarized THz pulse generation. In general, the single-atom picture can be applied to short (~millimeters) plasma lengths. However, when the plasma extends over centimeters, the single-atom picture loses its validity. First, due to air-plasma dispersion, the relative phase, θ, between the ω and 2ω pulses changes along the plasma. Furthermore, the 2ω pulse experiences a cross-phase modulation (XPM) induced by the stronger ω pulse and thus its polarization changes. These two parameters, θ and the polarization states of the optical pulses, have shown to affect the resultant THz polarization [20]. The modulations of these two parameters in turn change the direction of the local plasma current (thus THz polarization). Simultaneously, the optical and THz pulses propagate with different velocities in plasma, causing the local THz waves emitted from different parts of the plasma to arrive at different times in the far field. These two combined effects construct a THz pulse in the far field whose polarization direction rotates with time (see Fig. 16)

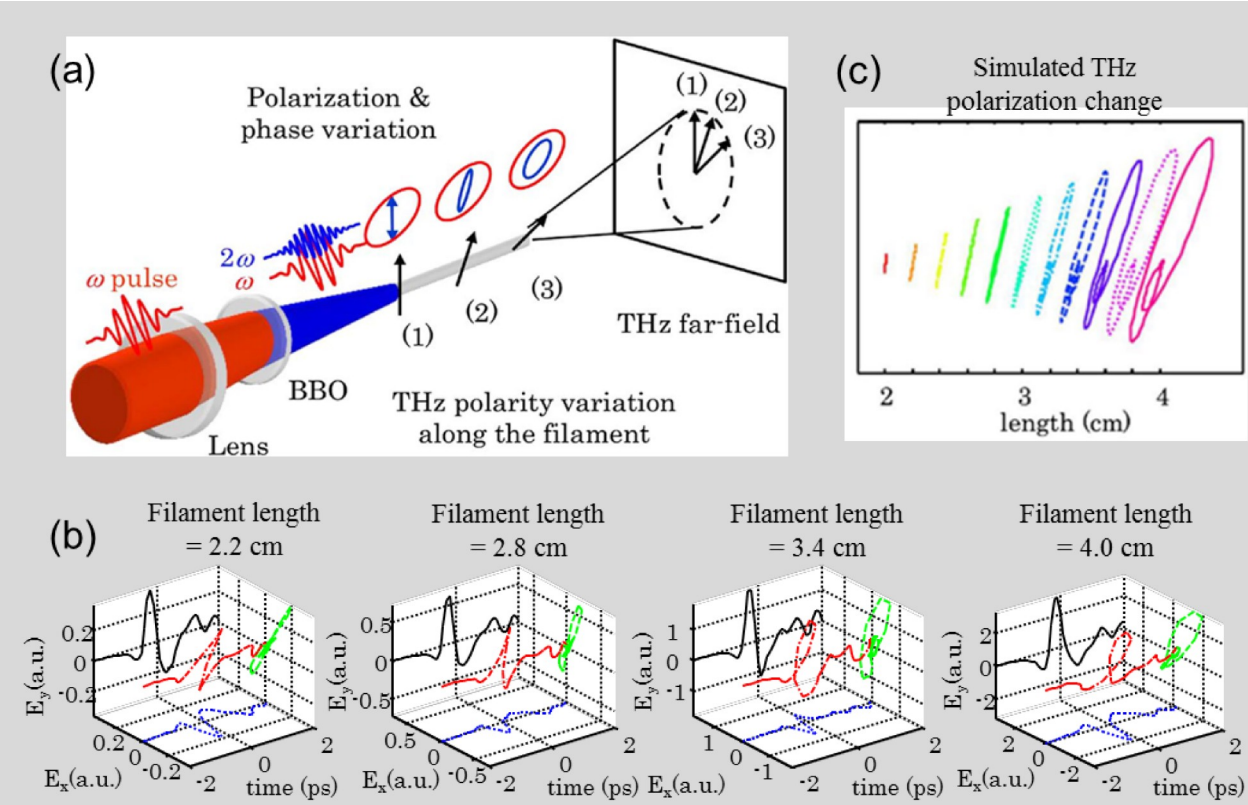

Figure 16. (a) Schematic of two-color (ω and 2ω) laser pulse propagation and THz polarization rotation. The THz far-field is constructed from successive time-delayed THz waves emitted with varying polarization. **(b)** Measurements of conversion from linear to elliptical THz polarization with increasing effective plasma filament length: 2.2 cm, 2.8 cm, 3.4 cm, and 4.0 cm. **(c)** Simulated THz polarization change with increasing propagation length.

Y. S. You, T. I. Oh, and K. Y. Kim, Opt. Lett. **38**, 1034 (2013).

6.4. THz generation from aligned molecules

Molecular ionization greatly depends on molecular orientation with respect to the laser electric field (polarization) [46-48]. Unlike atoms, molecules in general are not isotropic systems and their ionization rate can be strongly influenced by the angle between the laser field and the molecular axis. In the case of nitrogen, the ionization rate is 3~4 times higher when the molecular axis is aligned parallel to the laser polarization rather than perpendicular [47, 48]. Therefore, it is of great interest to investigate how THz radiation in two-color photoionization is influenced by molecular alignment during tunneling ionization. This provides a better understanding of THz generation mechanism and in particular, the role of tunneling ionization in THz generation. To experimentally investigate this phenomenon, one can perform a double-pulse experiment. Initially, an intense laser pulse aligns molecules through an impulsive rotational Raman excitation after which the alignment of molecules undergoes periodic field-free revivals [49]. Later, two-color laser pulses ionize the molecules at different timing of alignment revivals and the emitted THz can be probed (see Fig. 17).

Here, we report our experiments on molecular alignment-dependent THz radiation in two-color photoionization and explain the effect in the frame of plasma current model [10-12], establishing a link between THz radiation and alignment-dependent ionization. In particular, we have investigated how the molecular alignment of N_2 and O_2 can affect THz radiation in two-color photoionization (see Fig. 17(c)). Our experimental results show THz radiation is extremely sensitive to the alignment of molecules at the moment of tunneling ionization. This can be explained by the plasma current model combined with alignment-dependent ionization, in which air molecules aligned along the laser field, rather than randomly oriented, undergo more tunneling ionization with enhanced plasma currents, consequently yielding more THz radiation.

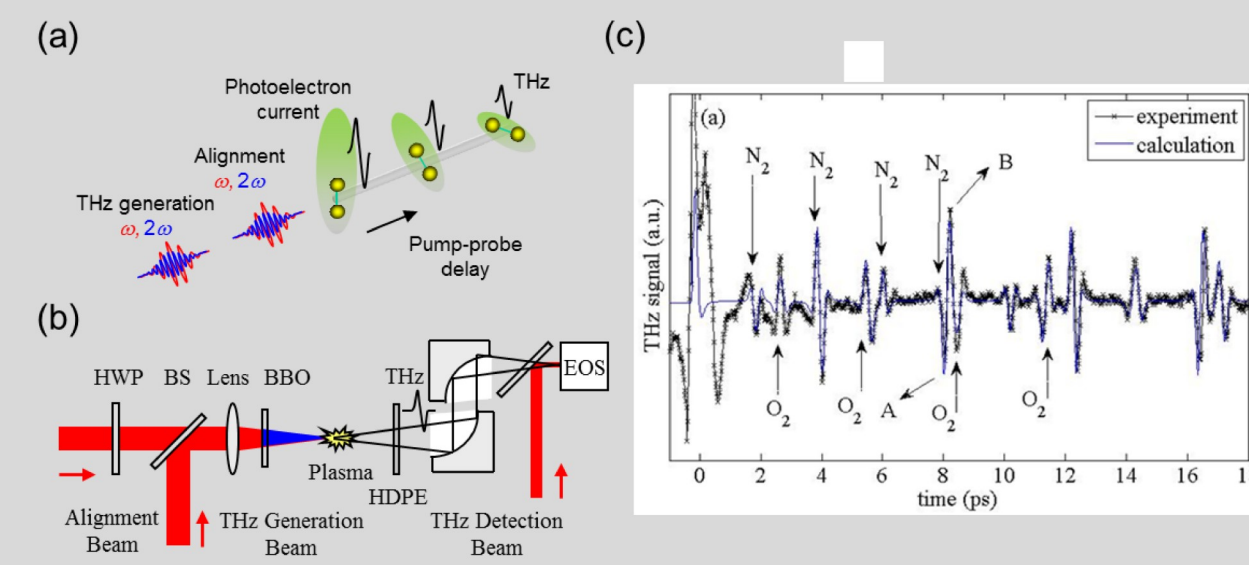

Figure 17. (a) Schematic of alignment-dependent photoionization of nitrogen molecules and resulting THz modulations in a pump-probe setup. **(b)** Experimental setup with three synchronous femtosecond laser beams for aligning molecules, generating and detecting THz radiation. HWP: half wave plate (optional), BS: beam splitter, BBO: β-barium borate crystal, HDPE: high-density polyethylene filter, EOS: electric-optical sampling for coherent THz detection. **(c)** Measured (black line with crosses) and simulated (blue line) THz output modulations versus delays.

Y. S. You, T. I. Oh, A. B. Fallahkahair, and K. Y. Kim, Phys. Rev. A **87**, 035401 (2013).

6.5. Strong THz field generation and real-time beam profiling

We have demonstrated high-field (>8 MV/cm) THz generation at a high-repetition-rate (1 kHz) via two-color laser mixing in air. Here we have used a cryogenically-cooled femtosecond laser amplifier capable of producing 30 fs, 15 mJ pulses at 1 kHz as a driver [25], along with a combination of a thin dual-wavelength half-waveplate [28] and a Brewster-angled silicon window to enhance terahertz generation and transmission (see Fig. 18(a)). In order to characterize the peak field strength, we have measured THz waveforms, energies, and spot sizes. In particular, we have used a microbolometer camera for real-time THz beam profiling and imaging (see Figs. 18(b-d)) [50-52]. This cost-effective THz camera along with our intense THz source can be a useful tool for nonlinear THz studies including broadband THz spectroscopy and imaging.

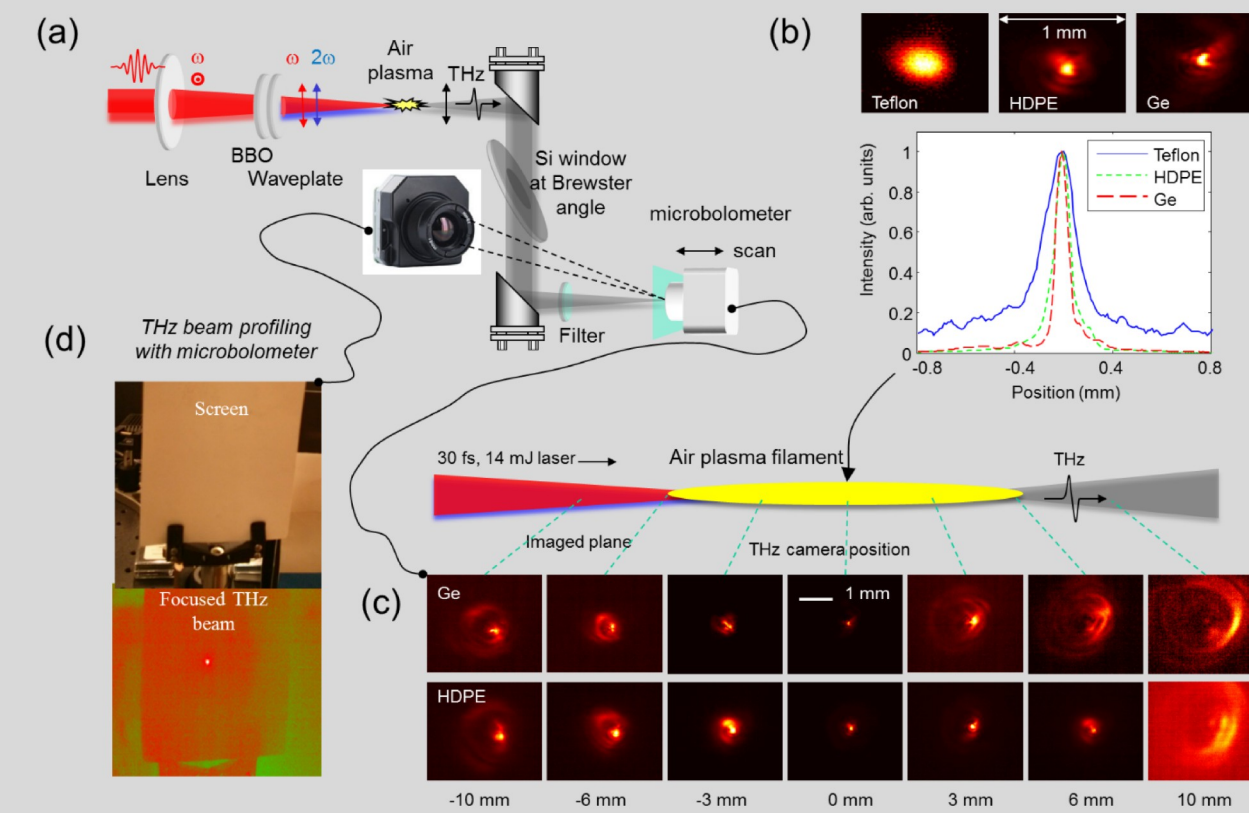

Figure 18. (a) Schematic of strong THz field generation via two-color laser filamentation in air and characterization. For maximal THz generation, a combination of a thin dichroic λ/2 waveplate and a large-size (4”), Brewster-angled Si window is used. For characterization, THz waveforms, energies, beam profiles are measured to determine the peak THz field strength (~8 MV/cm). For THz beam profiling, an uncooled microbolometer focal plane array is used with various filters in two different modes. For indirect beam profiling, a Ge lens is attached to the camera for imaging. **(b)** Focused THz beam profiles imaged by a microbolometer camera and their normalized central lineouts obtained with a 2-mm-thick Teflon (solid line), 2-mm-thick high-density polyethylene (HDPE) (dotted line), or 3-mm-thick germanium (thick dashed line) filter. **(c)** THz beam profiles obtained by a microbolometer camera at -10 mm, -6 mm, -3 mm, 0 mm, 3 mm, 6 mm, and 10 mm distances away from its best focus with an additional Ge transmission (<10 THz) or HDPE filter placed in front of the camera. **(d)** THz beams striking on a white screen (left), imaged by a microbolometer camera placed ~20 cm away from the screen with a germanium lens (7.5 mm diameter) attached in front.

T. I. Oh, Y. J. Yoo, Y. S. You, and K. Y. Kim, Appl. Phys. Lett. **105**, 041103 (2014).

7. Outlook and conclusion

Finally, we discuss the outlook for high-peak-power THz generation and theoretical limits in two-color photoionization in the filamentation regime (see Fig. 19(a)). Figure 19(b) summarizes THz energy scaling as a function of laser input energy. The black squares are our measurements obtained with various laser energy and filament length conditions. For given laser energy, there is a favorable filament length which yields the optimal THz conversion efficiency, 10^{-4}. This is represented as the straight line in Fig, 19(b). For instance, 10 mJ laser input energy will yield ~1 μJ THz energy with an optimal filament length of ~2 cm. 100 mJ laser energy will require a >15 cm long filament to produce ~10 μJ THz energy. An input of 1 J laser energy, achievable with a 30 TW laser system, will yield 100 μJ of THz energy with an estimated filament length of ~1.5 m (red diamond in the figure). The corresponding peak power will approach multi-GW with a 100 THz bandwidth.

The maximum achievable THz energy, however, is limited by the group velocity walk-off between two-color laser pulses. Due to air-plasma dispersion, two 50 fs pulses at 800 nm and 400 nm, for example, get separated in time as they propagate over ~4 m in air. This can produce ~300 μJ THz energy, a theoretical limit in two-color filamentation in air if the walk-off is not compensated.

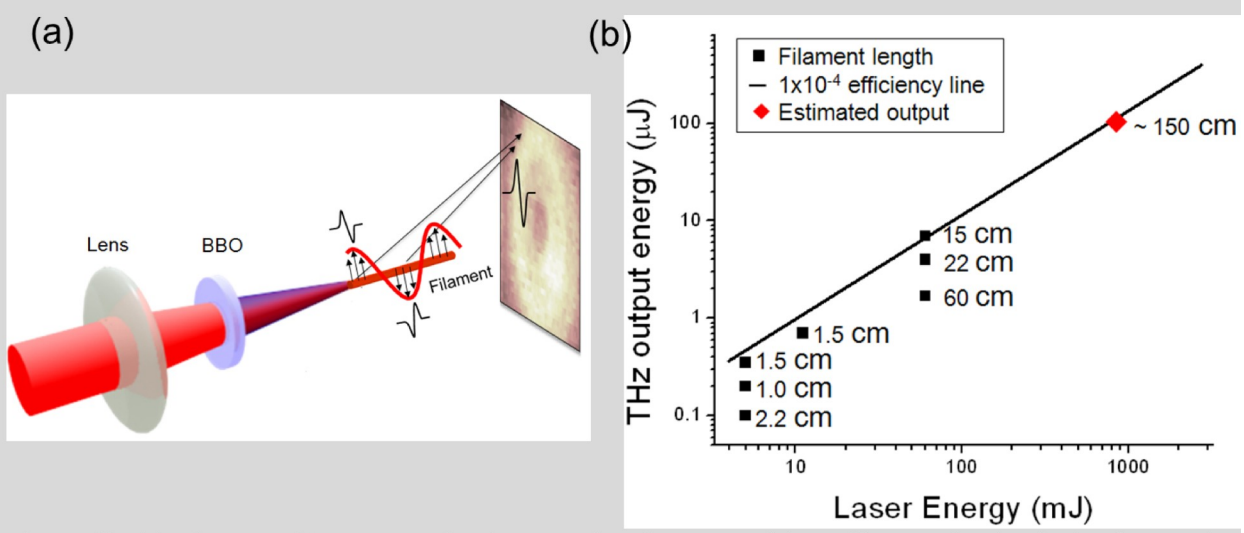

Figure 19. (a) Diagram of THz generation in two-color, femtosecond laser filamentation in air. A microscopic plasma current (blue dotted line), produced by the two-color electric field (red solid line) via tunneling ionization, emits THz radiation in all directions. However, the far-field THz radiation profile shown on the detection plane is determined by macroscopic interference between the THz waves emitted from the local THz sources distributed along the filament. This provides an off-axis phase-matching condition, yielding "**scala*b*le**" and "**conical**" THz radiation profiles. **(b)** THz output energy as a function of input laser energy with various air filament lengths (black squares). The straight line represents maximum achievable THz energy with a conversion efficiency of 10^{-4}. A ~1.5 m long filament made with 1 J can yield ~100 μJ THz. The ultimate THz output energy is limited to ~300 μJ by the group velocity walk-off between two-color laser pulses. Here the fundamental laser wavelength is assumed to be 800 nm.

T. I. Oh, Y. S. You, N. Jhajj, E. Rosenthal, H. M. Milchberg, and K. Y. Kim, New J. Phys. **15**, 075002 (2013).

Long filaments require a large parabolic mirror for THz energy collection. In addition, THz refocusing is another issue. One method in reducing the filament length while keeping the same high-energy THz output is to increase the plasma filament volume in the transverse direction. Focusing two-color laser pulses with a cylindrical lens can create a plasma sheet as shown in Fig. 20(a). For a laser input of 1 J, a plasma sheet of ~1 cm^2 can be created. For THz collection and refocusing, a combination of

a cylindrical mirror and a parabolic mirror can be used for tighter focusing. In addition, adaptive optics can be applied to produce THz fields exceeding 100 MV/cm [25] and demonstrate THz-induced tunneling ionization of atoms and THz-driven electron acceleration (see Fig. 20(b)). Such radiation will allow us to observe extremely nonlinear THz phenomena in a university laboratory.

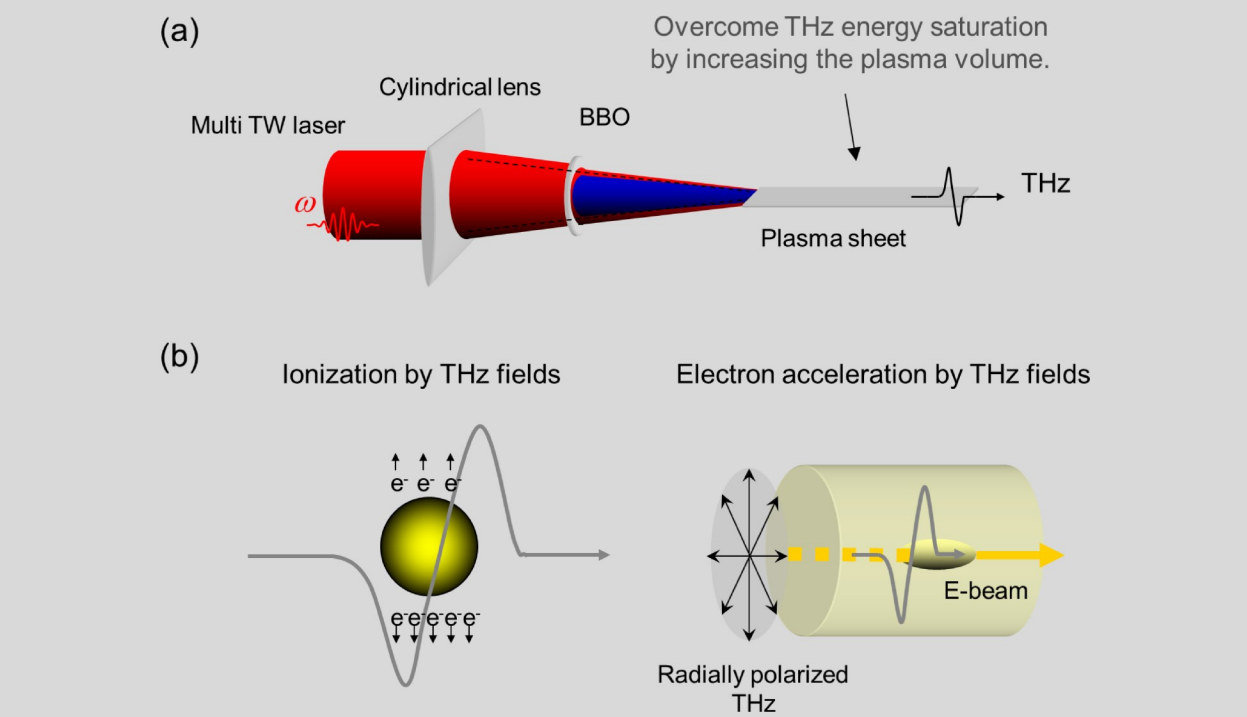

Figure 20. (a) Proposed experiment setup for scalable THz generation in a 2D plasma sheet using cylindrical lens focusing and recollection (not shown). **(b)** Examples of strong THz-field induced phenomena: tunneling ionization and electron acceleration.

Acknowledgement

The author thanks T. I. Oh, Y. S. You, Y. J. Yoo, N. Jhajj, E. W. Rosenthal, A. B. Fallahkhair, H. M. Milchberg, and L. A. Johnson, T. Rensink, J. P. Palastro, T. M. Antonsen, J. H. Glownia, A. J. Taylor, and G. Rodriguez for their discussions and contributions in conducting the experiments and simulations described in this report.

References

1. B. Ferguson and X. -C. Zhang, Nature Mater. **1**, 26 (2002).
2. M. Tonouchi, Nature Photon. **1**, 97 (2007).
3. Y. S. Lee, *Principle of Terahertz Science and Technology* (Springer, USA, 2008).
4. B. S. Alexandrov *et al*., Scientific Report **3**, 1184 (2013).
5. D. J. Cook and R. M. Hochstrasser, Opt. Lett. **25**, 1210 (2000).
6. M. Kress, T. Löffler, S. Eden, M. Thomson, and H. G. Roskos, Opt. Lett. **29**, 1120 (2004).
7. T. Bartel, P. Gaal, K. Reimann, M. Woerner, and T. Elsaesser, Opt. Lett. **30**, 2805 (2005).
8. X. Xie, J. Dai, and X.-C. Zhang, Phys. Rev. Lett. **96**, 075005 (2006).
9. J. Dai, X. Xie, and X.-C. Zhang, Phys. Rev. Lett. **97**, 103903 (2006).
10. K. Y. Kim, J. H. Glownia, A. J. Taylor, and G. Rodriguez, Opt. Express **15**, 4577 (2007).

11. K. Y. Kim, A. J. Taylor, J. H. Glownia, and G. Rodriguez, Nature Photon. **2**, 605 (2008).
12. K. Y. Kim, Phys. Plasmas **16** 056706 (2009).
13. H. Wen and A. M. Lindenberg, Phys. Rev. Lett. **103**, 023902 (2009).
14. J. Dai, N. Karpowicz, and X.-C. Zhang, Phys. Rev. Lett. **103**, 023001 (2009).
15. F. Blanchard, G. Sharma, X. Ropagnol, L. Razzari, R. Morandotti, and T. Ozaki, Opt. Express **17**, 6044 (2009).
16. Y. Liu, A. Houard, M.Durand, B. Prade, and A. Mysyrowicz, Opt. Express **17**, 11480 (2009).
17. T. -J. Wang, C. Marceau, S. Yuan, Y. Chen, Q. Wang, F. Theberge, M. Chateauneuf, J. Dubois, S. L. Chin, Laser Phys. Lett. **8**, 57 (2011).
18. E. Matsubara, M. Nagai, and M. Ashida, Appl. Phys. Lett. **101**, 011105 (2012).
19. K. Y. Kim, J. H. Glownia, A. J. Taylor, and G. Rodriguez, IEEE J. Quantum Electron. **48**, 797 (2012).
20. T. I. Oh, Y. S. You, and K. Y. Kim, Opt. Express **20**, 19778 (2012).
21. Y. S. You, T. I. Oh, and K. Y. Kim, Phys. Rev. Lett. **109**, 183902 (2012).
22. Y. S. You, T. I. Oh, and K. Y. Kim, Opt. Lett. **38**, 1034 (2013).
23. Y. S. You, T. I. Oh, A. B. Fallahkahair, and K. Y. Kim, Phys. Rev. A **87**, 035401 (2013).
24. T. I. Oh, Y. S. You, N. Jhajj, E. Rosenthal, H. M. Milchberg, and K. Y. Kim, Appl. Phys. Lett. **102**, 201113 (2013).
25. T. I. Oh, Y. S. You, N. Jhajj, E. Rosenthal, H. M. Milchberg, and K. Y. Kim, New J. Phys. **15**, 075002 (2013).
26. L. A. Johnson, J. P. Palastro, T. M. Antonsen, and K. Y. Kim, Phys. Rev. A **88**, 063804 (2013).
27. T. I. Oh, Y. J. Yoo, Y. S. You, and K. Y. Kim, Appl. Phys. Lett. **105**, 041103 (2014).
28. Y. Minami, T. Kurihara, K. Yamaguchi, M. Nakajima, and T. Suemoto, Appl. Phys. Lett. **102**, 041105 (2013).
29. M. Clerici, M. Peccianti, B. E. Schmidt, L. Caspani, M. Shalaby, M. Giguère, A. Lotti, A. Couairon, F. Légaré, T. Ozaki, D. Faccio, and R. Morandotti, Phys. Rev. Lett. **110**, 253901 (2013).
30. M. Clerici, D. Faccio, L. Caspani, M. Peccianti, E. Rubino, L. Razzari, F. Légaré, T. Ozaki, and R. Morandotti, Opt. Lett. **38**, 1899 (2013).
31. P. Klarskov, A. C. Strikwerda, K. Iwaszczuk, and P. Uhd Jepsen, New J. Phys. **15**, 075012 (2013).
32. V. Blank, M. D. Thomson, and H. G. Roskos, New J. Phys. **15**, 075023 (2013).
33. L. A. Johnson, J. P. Palastro, T. M. Antonsen, and K. Y. Kim, Phys. Rev. A 88, 063804 (2013).
34. A. Gorodetsky, A. D. Koulouklidis, M. Massaouti, and S. Tzortzakis, Phys. Rev. A **89**, 033838 (2014).
35. Z. Jiang and X. -C. Zhang, Appl. Phys. Lett. **72**, 1945 (1998).
36. K. Y. Kim, B. Yellampalle, G. Rodriguez, R. D. Averitt, A. J. Taylor, and J. H. Glownia, Appl. Phys. Lett. **88**, 041123 (2006).
37. K. Y. Kim, B. Yellampalle, A. J. Taylor, G. Rodriguez, and J. H. Glownia, Opt. Lett. **32**, 1968 (2007).
38. A. N. Chudinov, Y. E. Kapitzky, A. A. Shulginov, and B. Y. Zel'dovich, Opt. Quantum Electron. 23, 1055 (1991).
39. R. Stolle, G. Marowsky, E. Schwarzberg, and G. Berkovic, Appl. Phys. B 63, 491 (1996).
40. D. W. Schumacher, F. Weihe, H. G. Muller, and P. H. Bucksbaum, Phys. Rev. Lett. 73, 1344 (1994).
41. A. Couairon and A. Mysyrowicz, Phys. Rep. **441**, 47 (2007).
42. L. Berge, S. Skupin, R. Nuter, J. Kasparian, and J.-P. Wolf, Rep. Prog. Phys. **70**, 1633 (2007).
43. J. Kasparian and J.-P. Wolf, Opt. Express **16**, 466 (2008).
44. S. Chin, T. -J. Wang, C. Marceau, J. Wu, J. S. Liu, O. Kosareva, N. Panov, Y. P. Chen, J. -F. Daigle, S. Yuan, et al., Laser Physics **22**, 1 (2012).
45. J. Kasparian, R. Sauerbrey, and S. L. Chin, Appl. Phys. B **71**, 877 (2000).
46. Z. X. Zhao, X. M. Tong, and C. D. Lin, Phys. Rev. A **67**, 043404 (2003).
47. I. V. Litvinyuk, K. F. Lee, P. W. Dooley, D. M. Rayner, D. M. Villeneuve, and P. B. Corkum, Phys. Rev. Lett. **90**, 233003 (2003).
48. D. Pavičić, K. F. Lee, D. M. Rayner, P. B. Corkum, and D. M. Villeneuve, Phys. Rev. Lett. **98**, 243001 (2007).
49. Y.-H. Chen, S. Varma, A. York, and H. M. Milchberg, Opt. Express **15**, 11341 (2007).
50. A. W. Lee and Q. Hu, Opt. Lett. **30**, 2563 (2005).
51. N. Oda, C. R. Phys. **11**, 496 (2010).
52. A. Rogalski, Opto-Electron. Rev. **21**, 406 (2013).